Martian Dust Belts: Waiting for Discovery

Alexander V. Krivov

Astronomical Institute, St. Petersburg University, 198904 St. Petersburg, Russia
E-mail: krivov@aispbu.spb.su

and

Douglas P. Hamilton

Astronomy Department, University of Maryland, College Park, Maryland 20742–2421
E-mail: hamilton@astro.umd.edu

In this paper, we present modeling results of the presumed dust belts of Mars. We combine recently obtained theoretical results in dynamics of circumplanetary dust grains with up-to-date impact models and use a new numerical code to construct a three-dimensional, time-dependent, and size-dependent distribution of dust material. Our modeling is performed in two consecutive stages. First, for each grain size, we construct a relative spatial density distribution (i.e., a density distribution normalized to an arbitrary factor), which depends almost entirely on dust dynamics. We arrive at an extended set of data tables which quantitatively describe the asymmetric and season-dependent structure formed by different-sized grains. This step is done quite accurately using sophisticated dynamical models. Next, we model the dust production and loss rates in two conceivable formation scenarios to estimate absolute spatial dust densities. These results are uncertain by one or two orders of magnitude because the hypervelocity impact process is poorly characterized. We use the absolute spatial densities to estimate the normal and edge-on optical depths of the Phobos and Deimos tori and obtain values from 10^{-8} to 10^{-5}. Spacecraft data are required to substantially reduce these uncertainties. © 1997 Academic Press

1. INTRODUCTION

Twenty-five years ago Steven Soter (1971) first suggested that Mars should be surrounded by two tenuous dusty rings formed by the impact ejecta from the martian moons Phobos and Deimos. Since that time the putative belts of Mars, which still escape direct detection, were theoretically studied by many authors. In recent years, aspects of the problem have been addressed by Dubinin *et al.* (1990), Horányi *et al.* (1990), Ip and Banaszkiewicz (1990), Banaszkiewicz and Ip (1991), Horányi *et al.* (1991), Krivov *et al.* (1991), Andreev and Belkovich (1992), Ishimoto and Mukai (1992), Krymskii *et al.* (1992), Tátrallyay *et al.* (1992), Juhász *et al.* (1993), Kholshevnikov *et al.* (1993), Ishimoto and Mukai (1994), Krivov (1994), Krivov and Titov (1994), Sasaki (1994), Juhász and Horányi (1995), Baumgärtel *et al.* (1996), Błęcka and Jurewicz (1996), Hamilton (1996), Ishimoto (1996), Krivov and Krivova (1996), Krivov *et al.* (1996a,b), Sasaki (1996a,b), Orofino *et al.* (1997), Ishimoto *et al.* (1997), among others (see Hamilton 1996 for a detailed summary of previous results). These efforts have resulted in a vastly revised view of the martian dust rings; in particular, the orbital dynamics of dust around Mars is now well understood. Our aim in this work is to combine accurate orbital dynamics (Juhász and Horányi 1995, Hamilton 1996, Ishimoto 1996, Krivov *et al.* 1996a,b, Hamilton and Krivov 1996) with good impact ejecta models (Frisch 1992, Koschny and Grün 1996a,b) and a simulation technique (Krivov 1994) to estimate the spatial dust density in the martian tori quantitatively. In this paper, we synthesize these recent results and obtain the first predictions for optical depths and number densities of dust in the martian rings that are based on accurate orbital dynamics.

Estimating the spatial dust density within the rings is not an easy task since the martian rings are predicted to be asymmetric and time variable (Hamilton 1996) and to contain a distribution of particle sizes. Nevertheless, such models are strongly needed in view of upcoming exploration of the red planet by a fleet of American, European, Japanese, and Russian spacecraft (see, e.g., Galeev *et al.* 1996 a,b, Huntress *et al.* 1996, Tsuruda *et al.* 1996 for an outline of the international strategy of Mars exploration and descriptions of individual missions). We hope that our results will be used by spacecraft mission teams to design onboard dust experiments and by mission planners to make quantitative risk assessments.

Like dust complexes in the vicinities of the jovian planets, the theoretically predicted dust belts of Mars are expected to consist of several populations with quite distinct features (Juhász *et al.* 1993, Krivov 1994). The biggest ejecta fragments, larger than approximately 1 mm, are confined to narrow tori, whose dimensions are controlled by initial ejection velocities (Soter 1971, Kholshevnikov *et al.* 1993). These macroscopic grains should be rapidly reaccreted by the parent moon and hence are present with very low number densities. The particles from tens to hundreds of micrometers in size can stay in orbits near Mars for tens to tens of thousands of years and should form the most perceptible component of martian dust environment (population I in the terminology of Krivov 1994). These grains form extended tori around the orbits of Phobos and Deimos. Particles with radii smaller than a critical value r_{cr} (30 μm for Phobos and 14 μm for Deimos, see Krivov *et al.* 1996b), but greater that about 1 μm, swiftly hit Mars as a result of radiation pressure and Mars' oblateness perturbations. These small grains form population II. Still smaller, submicrometer-sized grains are subject to fast unpredictable orbital changes in the solar wind flows, and form an extended, low-density, and highly variable ethereal halo around Mars (Horányi *et al.* 1990, 1991), called population III by Krivov (1994). In this paper, we focus on grains from 1 to 100 μm in size, i.e., on populations I and II.

Our modeling is broken down into two steps. For dust grains of a given size, we first construct the relative (e.g. normalized to an arbitrary factor) spatial dust density distribution in Section 2. The results provide a quantitative description of the asymmetric, season-dependent, and size-dependent geometry of the martian dust belts. In the second step, we calculate the absolute concentrations of particles (Section 3). Here, for each grain size, we estimate the ejecta production rate from the satellite surfaces and the efficiency of particle loss mechanisms. We obtain estimates of absolute number densities of dust, optical depths, and other parameters of the tori. These results are compared with those obtained by other authors.

2. SPATIAL DENSITY DISTRIBUTIONS FOR DUST

2.1. Single-Particle Dynamics

Several recent studies (Juhász and Horányi 1995, Hamilton 1996, Ishimoto 1996, Krivov *et al.* 1996a,b, Hamilton and Krivov 1996) have shown that the dynamics of Phobos and Deimos ejecta larger than about 1 μm are governed primarily by the coupling of solar radiation pressure and Mars' oblateness perturbations. There are at least three approaches to studying the problem: (1) direct numerical integration of Newton's second law in rectangular coordinates; (2) numerical integration of orbit-averaged equations for orbital elements; (3) approximate analytical solutions of the orbit-averaged equations of motion. We choose the second possibility, which provides reasonably accurate results (see Krivov *et al.* 1996b for estimates of accuracy) without prohibitively long computing times (direct integrations in coordinates are about two orders of magnitude slower). We numerically integrate the orbit-averaged equations of motion derived in Krivov *et al.* 1996b [Eqs. (17)–(20)]; these equations are written in Lagrangian elements that are well defined for low eccentricities and inclinations. As the independent variable, we use the solar longitude $\lambda_\odot$, measured in the planet's orbital plane from the vernal equinox point. The solar longitude is a linear function of time, if we neglect the eccentricity of the martian orbit about the Sun ($e_M = 0.093$). This approximation is reasonably good for Deimos ejecta, but the martian eccentricity causes appreciable changes to the orbits of some Phobos particles (Hamilton 1996). The assumption $e_M = 0$ is a shortcoming of our model.

Using the equations described above implies some additional, but less restrictive, simplifications. We ignore all forces other than direct solar radiation pressure and Mars' oblateness perturbations and assume that the semimajor axis of a particle's orbit is equal to that of the parent satellite orbit, since neither radiation pressure nor planetary oblateness produces secular changes in this element. We also assume that the particle's initial orbit is circular ($e_0 = 0$) and that it lies in the equatorial plane of Mars ($i_0 = 0$), thereby neglecting both (1) the small eccentricities and inclinations of Phobos and Deimos and (2) the initial ejecta velocities from each moon. These are all excellent approximations for dust grains smaller than about 100 μm in radius (Hamilton 1996, Krivov *et al.* 1996b).

2.2. From One Particle to Ensemble of Grains

Hamilton (1996) showed that the structure of the martian rings should vary periodically in time as Mars orbits the Sun. This causes the configuration of the martian dust complex to be, in our notation, a 2π periodic function of the solar longitude, $\lambda_\odot$. To construct the time-dependent relative density distribution in the martian tori, we proceed as follows.

1. Fix the parent moon (Phobos or Deimos) and the grain size r_g.

2. Fix the martian season (solar longitude) $\lambda_\odot^*$ of interest; we adopt that the martian vernal equinox occurs at $\lambda_\odot = 0$. More precisely, we fix a (narrow) interval of width $\Delta \lambda_\odot^*$ centered on $\lambda_\odot^*$, where $\Delta \lambda_\odot^*$ is the "resolution" of our model.

3. We launch N_{traj} dust particles at different time instants distributed uniformly in one martian year. In the other words, we take a uniform grid of ejection moments t_0 between $t = 0$ and $t = 1$ martian year or, equivalently, choose a uniform set of initial solar longitudes $\lambda_\odot$ between $\lambda_\odot = 0$ and $\lambda_\odot = 2\pi$. We take $\lambda_\odot (t = 0) = 0$.

4. Each of N_{traj} trajectories is integrated from t_0 to $t_0 +$ t_{interval} with printout step t_{step}. For population I, t_{interval} is chosen long enough to cover possible long-term variations of orbital elements. For example, since the inclinations of Deimos particles change with periods of tens of martian years (Krivov *et al.* 1996b), we need to take t_{interval} of order 100 martian years to allow the particles to develop maximum inclinations, otherwise the torus thickness will be underestimated. For population II, t_{interval} can be chosen to be much shorter, on the order of a martian year.

5. Orbital elements, which describe the shape of an instantaneous Keplerian ellipse, are printed out regularly along each of the calculated trajectories. For each set of orbital elements, we assign N_{points} random values to the mean anomaly M and transform the orbital elements to Cartesian coordinates. This step takes advantage of the fact that the perturbation forces are weak compared with Mars' gravity to produce a realistic distribution of dust along each of the instantaneous Keplerian ellipses.

6. Finally, we retain only those modeled grain positions that correspond to our chosen martian season $\lambda_{\odot}^{*}$, (i.e., only those positions where $\lambda_{\odot}$ satisfies the inequality $\lambda_{\odot}^{*} - \Delta\lambda_{\odot}^{*}/2 \leq \lambda_{\odot} \leq \lambda_{\odot}^{*} + \Delta\lambda_{\odot}^{*}/2$, with all angles in the range $[0, 2\pi]$).

The total number of modeled grain positions N_{modeled} is estimated as

$$N_{\text{modeled}} \approx \frac{\Delta\lambda_{\odot}^{*}}{360°} \times N_{\text{traj}} \times \frac{t_{\text{interval}}}{t_{\text{step}}} \times N_{\text{points}}. \quad (1)$$

If lifetimes of the particles are shorter than t_{interval} (this is the case for the grains of population II), the typical lifetime should be used instead of t_{interval} in Eq. (1).

2.3. Ensemble of Grains: Geometry of the Tori

Studying the large grains of population I, we performed modeling calculations for the following grain sizes: (32, 40, 50, 60, and 80 μm (Phobos) and 17, 25, 40, 60, and 80 μm (Deimos). In our calculations, we assume a material density of $\rho_g = 2.0$ g cm^{-3} and a radiation pressure efficiency of $Q_{\text{pr}} = 1.0$. The minimum grain radii are taken to be just above the critical values 30 μm (Phobos) and 14 μm (Deimos)—smaller grains rapidly collide with Mars at the pericenters of their orbits. We have taken the following values of the modeling parameters explained above: N_{traj} = 10, t_{interval} = 100 martian years, t_{step} = 0.023 martian years, N_{points} = 3, $\Delta \lambda_{\odot}^{*}$ = 20°, so that we expect N_{modeled} $\sim$ 7200 from Eq. (1). In reality, the actual number of numerically-determined points differed from N_{modeled} by up to a few percent.

In Figs. 1–4, we display "snapshots" of the tori, for Phobos dust with r_g = 32 μm (Fig. 1) and 80 μm (Fig. 2)

and Deimos dust with r_g = 17 μm (Fig. 3) and 80 μm (Fig. 4). Each figure contains the views of the dust tori for four martian seasons—spring ($\lambda_{\odot}$ = 0°), summer ($\lambda_{\odot}$ = 90°), autumn ($\lambda_{\odot}$ = 180°), and winter ($\lambda_{\odot}$ = 270°)—in three orthogonal projections (*XY, XZ,* and *YZ* in the equatorial inertial frame, with the *X* axis being directed toward the vernal equinox point).

For population II, we made calculations for the following sizes: 1, 5, 15, and 25 μm (Phobos) and 1, 5, 7, and 12 μm (Deimos). Other modeling parameters were taken as follows: N_{traj} = 100, t_{interval} = 1 martian year, t_{step} = 0.0023 martian years, N_{points} = 10, $\Delta \lambda_{\odot}^{*}$ = 20°. Figures 5 and 6 depict scatter plots for Phobos and Deimos dust with the sizes given above. The figures contain the views of the dust tori for martian spring equinox in three orthogonal projections.

2.4. Discrete Representation of the Dust Density

To simplify calculations of measurable quantities, such as light scattering by the dust complex, we also converted the relative density distributions into a set of "digital tables." Our computer code scans a list of modeled grain positions and distributes them over a grid of spatial bins, determined by the user, and then counts the numbers of grain occurrences in these bins. Figure 7 illustrates results for 32-μm Phobos dust during the vernal equinox (cf. upper left panel in Fig. 1). The *XY* plane contains 20 × 20 cells, and no division into *Z*-layers is necessary (because the Phobos torus is very thin). These digital tables, or torus slices, have been calculated for both moons, for a wide range of grain sizes, for different martian seasons, and for different spatial resolutions.

We also present similar data in the form of a contour plot that gives isolines of number density of dust (Fig. 8). Figure 8 is drawn for similar conditions as Fig. 7 (32-μm Phobos dust during the vernal equinox, one *Z* layer), but is based on a larger number of points ($N_{\text{modeled}} \approx$ 162,000) and on a more detailed spatial grid (50 × 50 bins). Such contour plots can easily be calculated for different-sized ejecta from both satellites and for different martian seasons.

2.5. Typical Features of the Martian Dust Tori

Figures 1–4 (or their digital counterparts like Fig. 7 or contour plots like Fig. 8), together with similar pictures drawn for other grain sizes, allow one to see the prominent features of the tori (population I). We find, as have other previous studies (Hamilton 1996, Ishimoto 1996, Krivov *et al.* 1996b), the following key features:

1. Both Deimos and Phobos tori change from one martian season to another, but the dependence is more pronounced for the Deimos belt. The Deimos torus is displaced away from the Sun, whereas the Phobos torus is
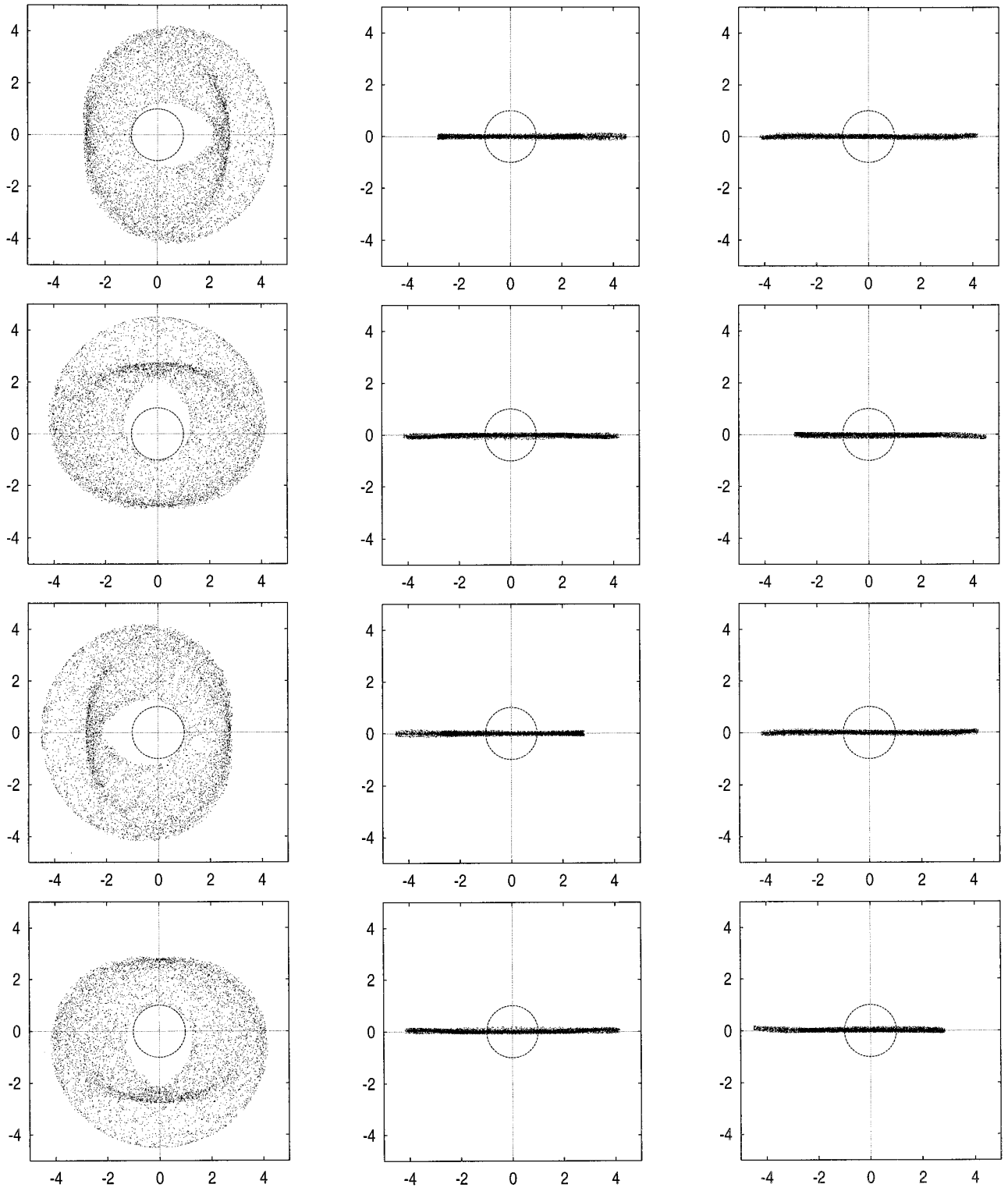
FIG. 1. Snapshots of the Phobos torus formed by 32-μm particles. The torus is shown in three projections (XY, XZ, and YZ from the left to the right) and for four martian seasons (from spring equinox at the top to winter solstice at the bottom). The coordinate system is centered on Mars, with the X axis directed toward the martian spring equinox and the Z axis pointing to the martian north pole. The unit of distance is Mars' radius.
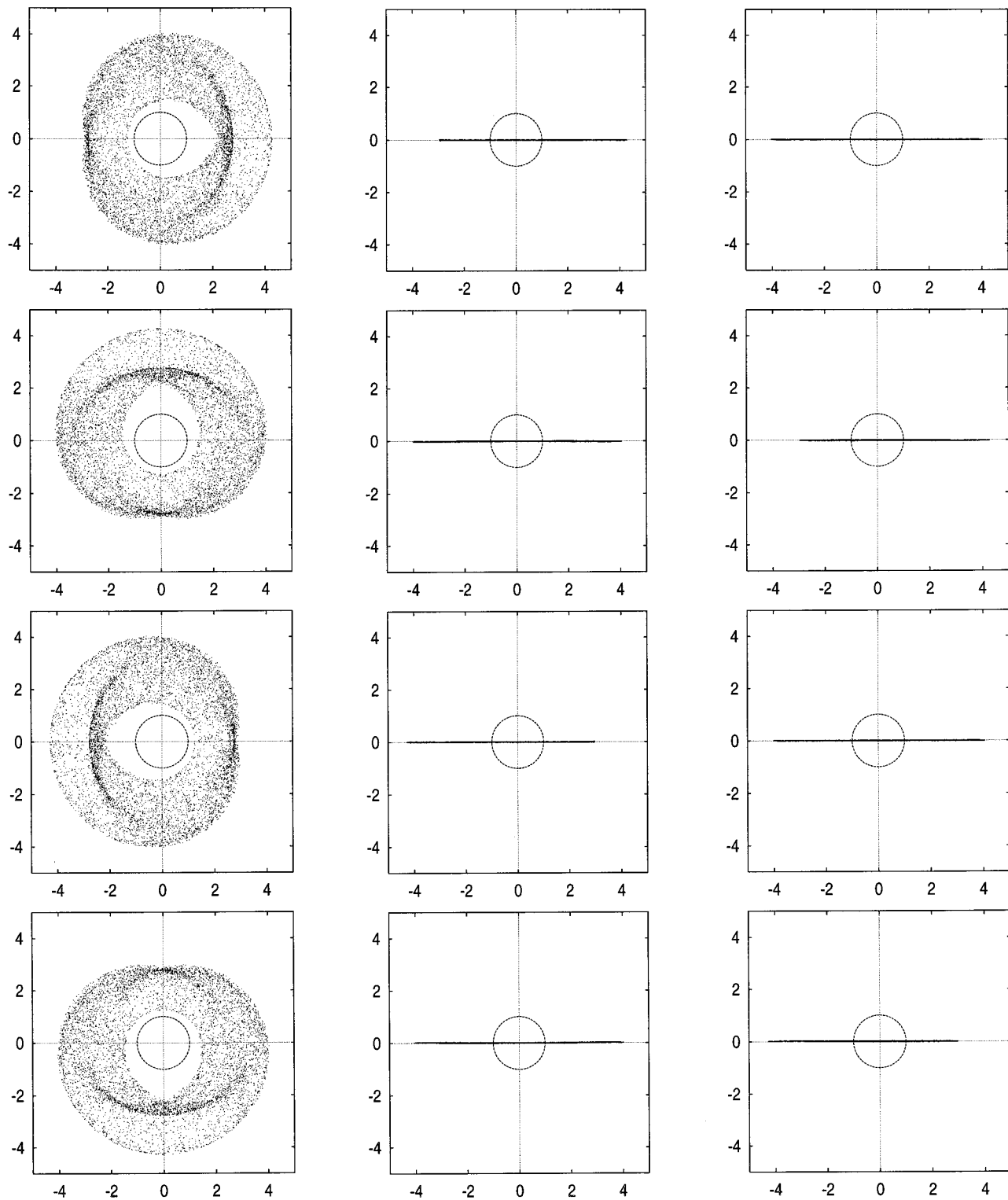
FIG. 2. Same as in Fig. 1, but for 80-μm Phobos particles.
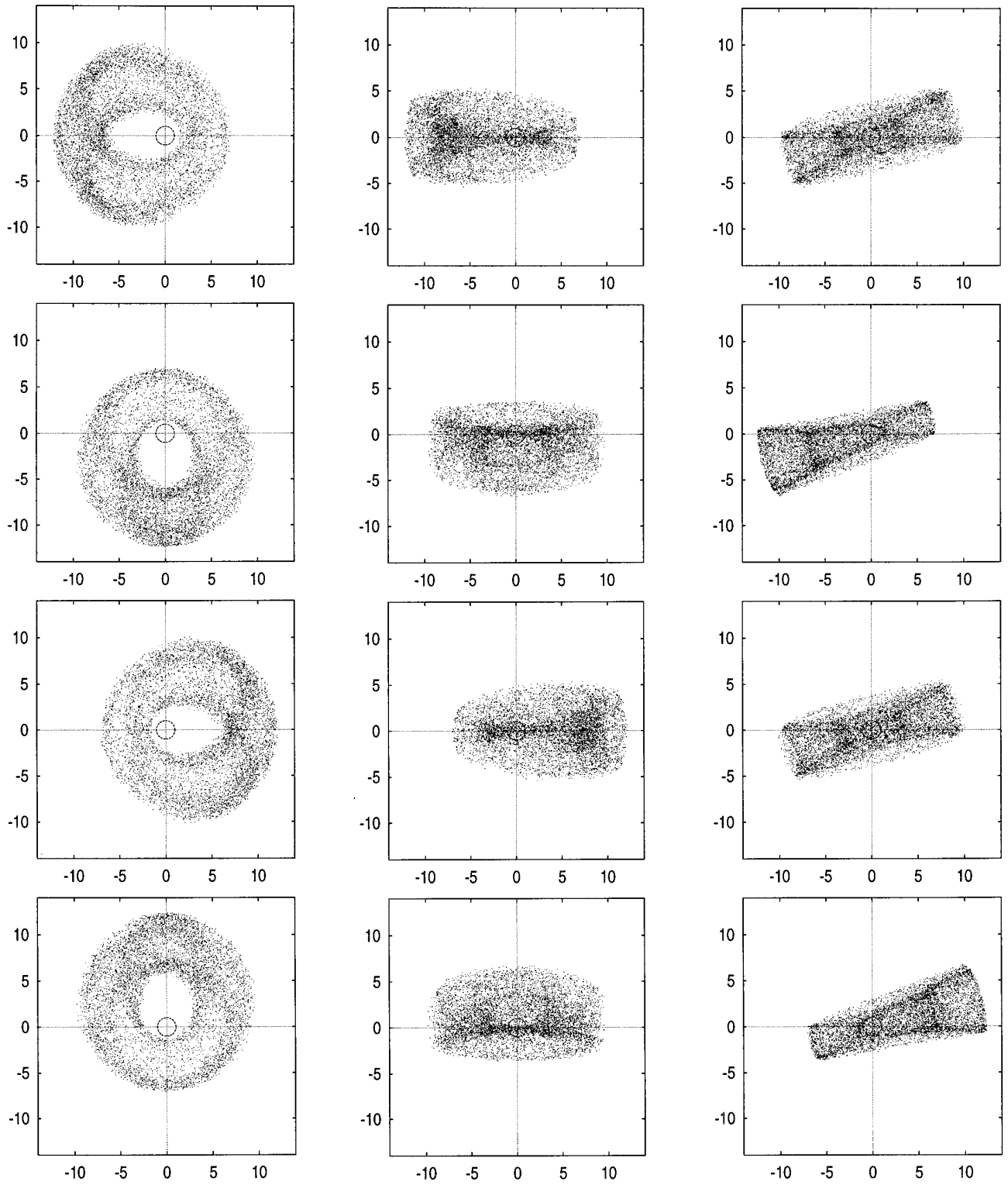
FIG. 3. Same as in Fig. 1, but for 17-μm Deimos particles.
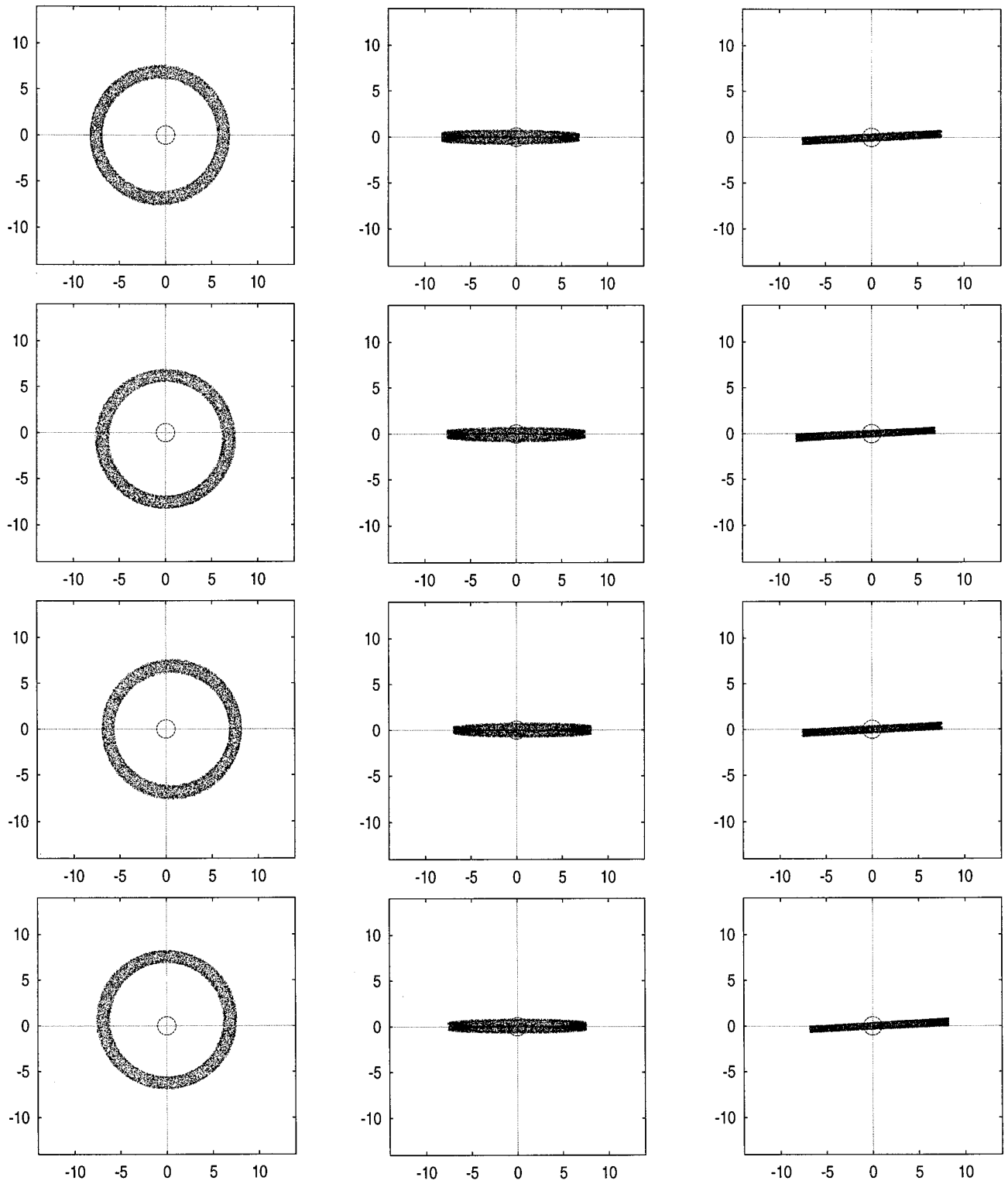
FIG. 4. Same as in Fig. 1, but for 80-μm Deimos particles.
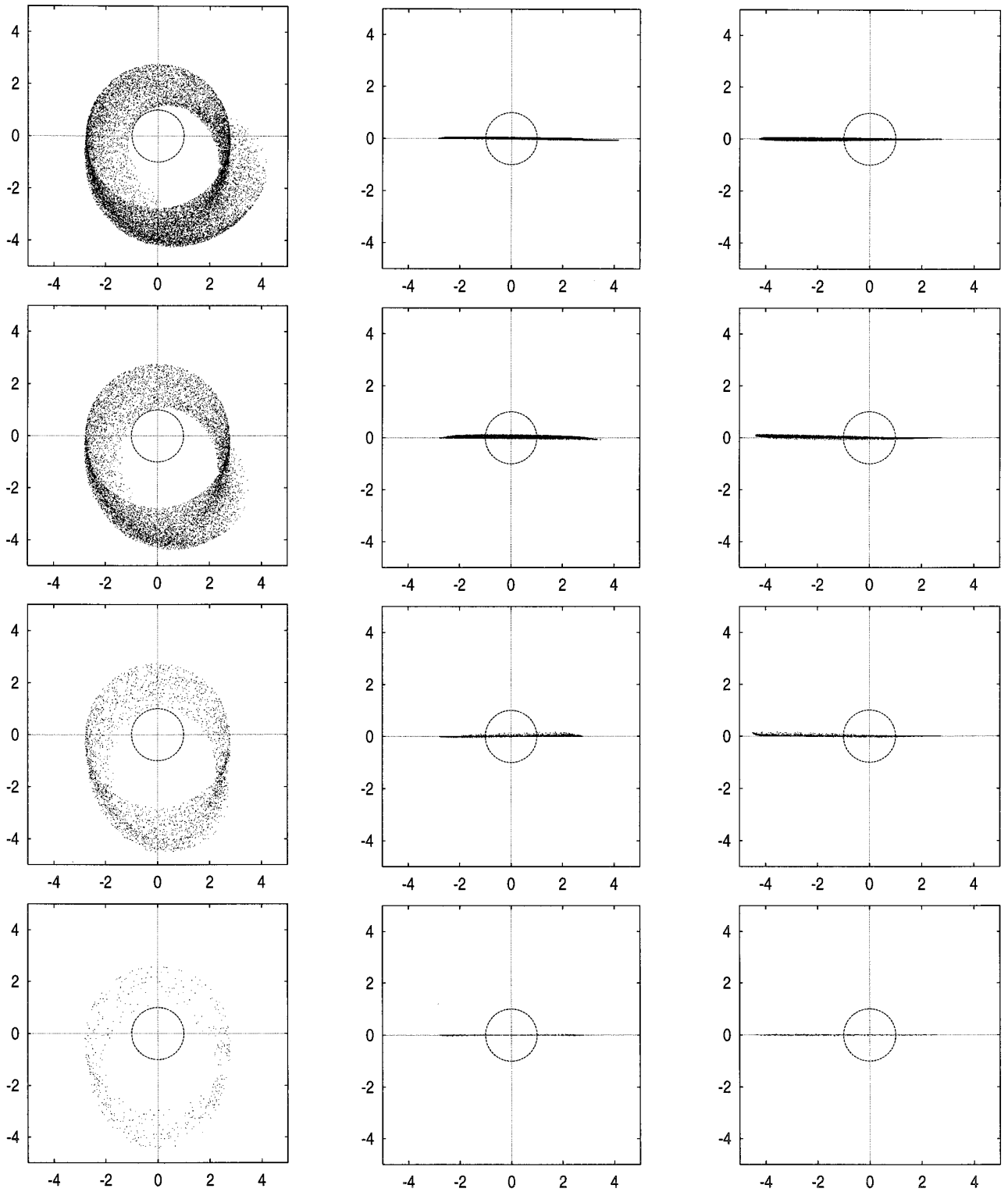
FIG. 5. Snapshots of the Phobos torus formed by particles with radii smaller that the critical size 30 μm: 25, 15, 5, and 1 μm from top to bottom. The ring is shown in three projections (*XY*, *XZ*, and *YZ* from the left to the right) of the same coordinate system as in Figs. 1–4. All panels are drawn for martian spring equinox.
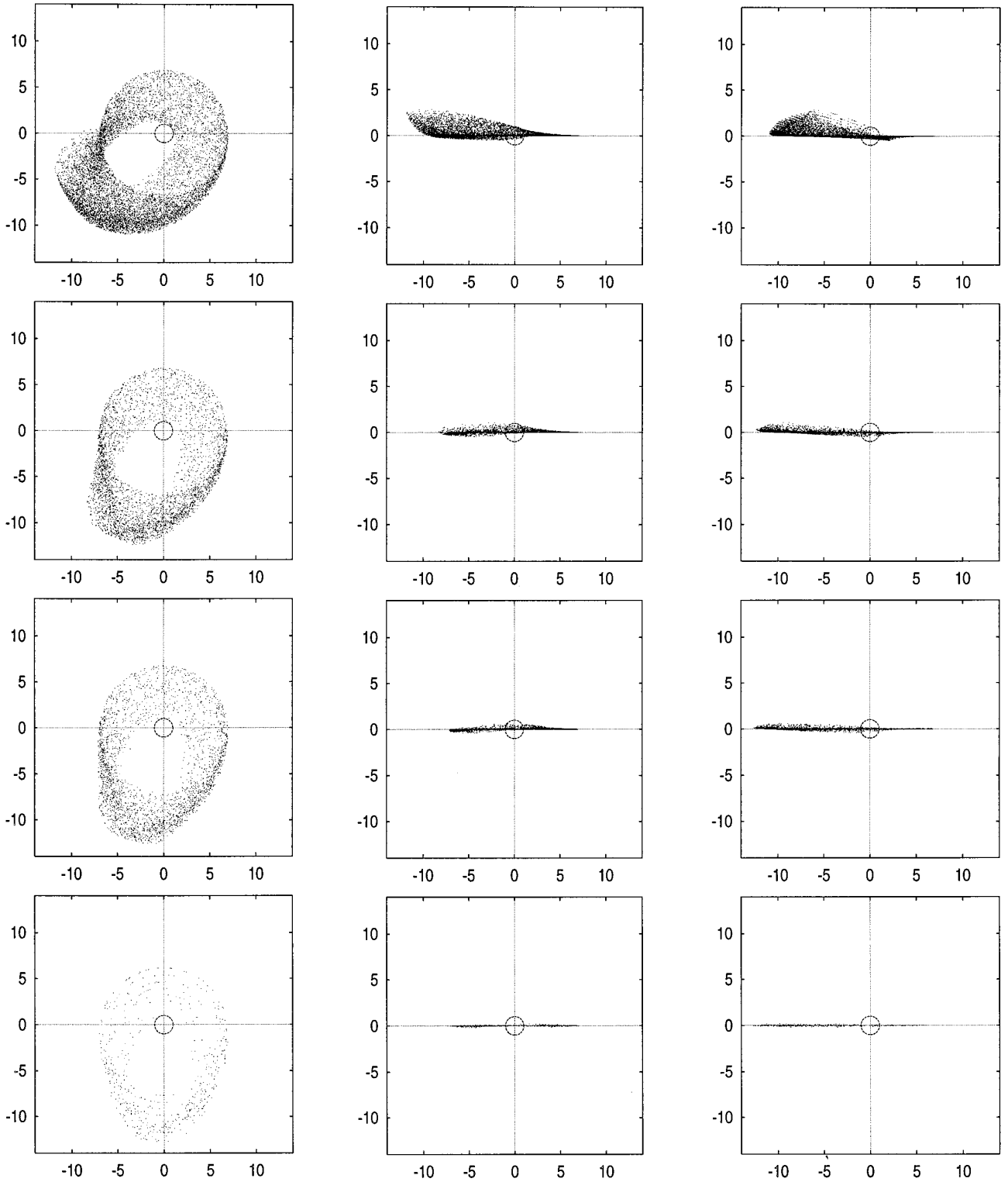
FIG. 6. Snapshots of the Deimos torus formed by particles with radii smaller that the critical size 14 μm: 12, 7, 5, and 1 μm from top to bottom. Three projections from the left to the right are the same as in Fig. 5. All panels are given for martian spring equinox.

```
o   o   o   o   o   o   o   o   o   o       o   o   o   o   o   o   o   o   o
o   o   o   o   o   o   o   o   o   9  19  28  19   o   o   o   o   o   o   o
o   o   o   o   o   o   o  18  56  63  49  49  50  51  24   3   o   o   o   o
o   o   o   o   o   o  43  59  35  38  50  40  44  42  29  32   9   o   o   o
o   o   o   o   o  24  53  34  27  28  31  40  32  48  35  21  25   7   o   o
o   o   o   o   7  56  33  34  25  22  29  31  27  53  65  27  26  34   o   o
o   o   o   o  25  53  53  27  23  27  21  39  28  26  85  31  15  23  11   o
o   o   o   o  79  60  32  32  17  24  24  27  35  26  71  78  14  22  31   o
o   o   o   o  92  45  21  25  19   o   o   o   6  28  49  86  18  14  17   o
o   o   o   o 105  41  24  29   5   o   o   o   o   2  79  91  12  16  23   3
o   o   o   o  93  42  30  28   1   o   o   o   o   2  69 102  15  22  27   o
o   o   o   o  72  46  24  12  17   o   o   o   1  40  68  75  11  16  21   o
o   o   o   o  57  44  38  31  27  20  19  34  36  31  52  69  18  21  23   o
o   o   o   o  17  63  26  31  14  33  21  25  25  32  84  37  14  35  10   o
o   o   o   o   5  70  50  32  27  33  25  24  30  38  68  20  19  24   o   o
o   o   o   o   o  18  62  43  41  27  29  24  47  56  36  18  28   9   o   o
o   o   o   o   o   o  29  66  50  46  48  37  46  37  23  29  10   o   o   o
o   o   o   o   o   o   o  22  59  50  49  59  34  46  25   1   o   o   o   o
o   o   o   o   o   o   o   o   o  10  16  23  13   o   o   o   o   o   o   o
o   o   o   o   o   o   o   o   o   o   o   o   o   o   o   o   o   o   o   o
```

FIG. 7. Phobos torus formed by 30- to 35-μm particles at the instant of martian vernal equinox, in "digital" form. The numbers give relative dust densities of the torus at locations near Mars. The table covers area of 10×10 martian radii in the equatorial plane of Mars; the planet is at the center of the table. The size of each cell is $0.5 \times 0.5 \times 0.5$ martian radii. The absolute number of grains contained in any cell can be obtained by Eq. (2). In this example, $N = 4 \times 10^{14}$ (see Table II) and $N_{\text{modeled}} = 7194$. So, the expected number of grains in any spatial bin is the number written in the table multiplied by $N/N_{\text{modeled}} \approx 6 \times 10^{10}$.

shifted toward the Sun. Smaller grains show larger displacements.

2. The Phobos dust belt is very thin and is more accurately called a ring than a torus. The sizes and shapes of the "partial" rings formed by different-sized Phobos ejecta exhibit a weak dependence on the grain radii. The Deimos torus, in contrast, is highly extended in the vertical direction. Smaller grains form thicker tori.

3. The Phobos ring is confined to the martian equatorial plane, but the plane of symmetry of the Deimos torus is tilted relative to the equator. This plane is always seen edge-on in the YZ projection (see right panels in Figs. 3 and 4). The tilt angle varies from 3° for $r_g = 80$ μm to 18° for $r_g = 17\mu$m. Furthermore, the Deimos torus is not rotationally-symmetric (its thickness varies with longitude).

4. There are peculiar jumps in density within the Phobos

torus ("caustics") observed in the left panels in Figs. 1 and 2. The same is clearly seen in Figs. 7 and 8 as well. The effect can be explained by near-resonant effects of Phobos dust dynamics (Hamilton 1996). We also observe that the distribution of dust in the Deimos torus is very non-uniform, especially in the vertical direction (middle and right panels in Fig. 3). This feature has not been emphasized in previous works.

Similarly, Figs. 5 and 6 (or their digital counterparts, not reproduced in this paper) show typical features of the population II formed by smaller particles. We can draw the following conclusions on the structure of this component of the martian dust environment.

1. The azimuthal structures of the tori in Figs. 5 and 6 bear clear signs of the short lifetimes of small particles. Radiation pressure causes the solar angle (the angle be-
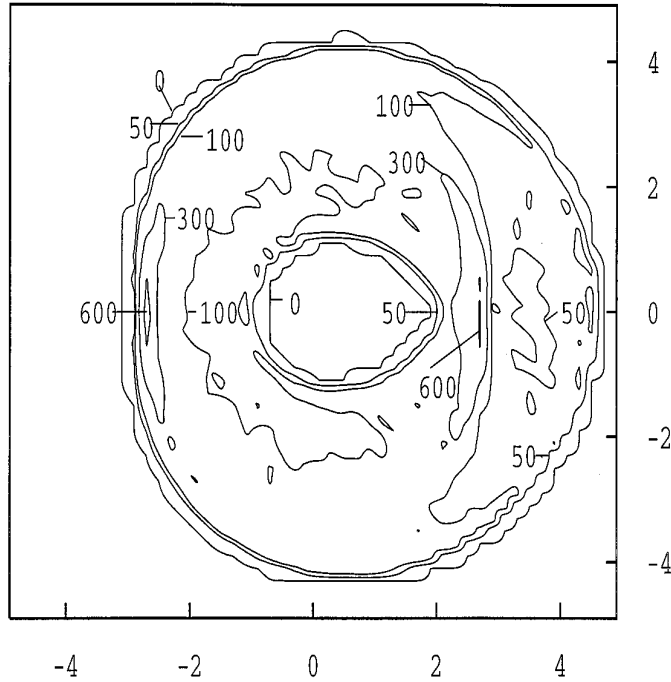
FIG. 8. Phobos torus formed by the same particles, at the same season and for the same area in the equatorial plane of Mars as in Fig. 7, but in the form of a contour plot. Densities in the legend are given in relative numbers; the absolute number density of grains at any spatial location can be calculated by Eqs. (2) and (3). For this plot, $N = 4 \times 10^{14}$ as in Fig. 7; $N_{\text{modeled}} \approx 162{,}000$; the size of each cell was $0.2 \times 0.2 \times 0.2$ martian radii. (The vertical size of the bin of 0.2 martian radius roughly equals the average semi-thickness of the torus.) The expected number density (km^{-3}) of grains is the number assigned to an isoline multiplied by $N/N_{\text{modeled}}/V_{\text{bin}} \approx 0.8$, so that our relative numbers can be interpreted as absolute number densities (in km^{-3}). Thus the maximum relative density (700–800) translates to an actual number density of $\approx$600 km^{-3}.

tween the directions toward the pericenter and the Sun) of the initially circular grain orbits to spin instantaneously to 90°. The solar angle then changes (it decreases for Deimos grains and increases for Phobos dust—see Hamilton 1996) as the eccentricity grows, until the critical eccentricity is attained and the dust grain strikes Mars. These effects can be seen in the left panels of Figs. 5 and 6: the dust distributions are not symmetric about the y axis, and the most distant material is located to the bottom right (left) of the y axis for Phobos (Deimos) as is expected from the behavior of the solar angle. For the smallest particles, which end their life very rapidly, the solar angle remains near its starting value of 90° (bottom panels in Figs. 5 and 6).

2. The vertical structures of the small debris rings of Phobos and Deimos also show some curious features. Depending on the season, small particles launched from Phobos and Deimos can reach maximum inclinations from 1° to 8° and from 3° to 30°, respectively, before they collide with Mars (Hamilton 1996). During most seasons, small grains ($r_g < 30\ \mu$m) from Phobos will extend further vertically than larger grains. Conversely, small grains ($r_g < 14\ \mu$m) from Deimos nearly always form a flatter distribution than the larger grains.

3. ABSOLUTE DENSITY DISTRIBUTIONS FOR DUST

3.1. Steady-State Number of Torus' Particles

We now normalize the relative dust densities for a given grain size to absolute ones, i.e. to actual dust concentrations at different locations near Mars. For a given grain size, it is sufficient to calculate just one number for each of the dust distributions—an estimated total number N of grains contained in the steady-state dust torus. Given this number, one can immediately calculate the absolute number of particles enclosed in a given spatial bin, N_{abs}, as

$$N_{\text{abs}} = \frac{N_{\text{rel}}}{N_{\text{modeled}}} \times N, \tag{2}$$

where N_{rel} is the relative number of points calculated by the binning program and N_{modeled} is given by Eq. (1). For example, N_{rel} could be a number written in a given cell in Fig. 7 in which case N_{modeled} would be the sum of all the numbers is Fig. 7. The mean number density of dust particles in the bin with the volume V_{bin} will be simply

$$n_{\text{abs}} = \frac{N_{\text{abs}}}{V_{\text{bin}}}. \tag{3}$$

All of the physics, namely, a quantitative assessment of sources and sinks of dust and the particle loss processes, is contained in the calculation of N, which plays the role of a scaling factor in our model. We now describe how N is calculated in two different scenarios.

3.2. Interplanetary Impactor Scenario

We start with a discussion of the classic way in which material can be supplied to the dust tori: the bombardment of martian satellites by interplanetary particles, as first suggested by Soter (1971). We call this formation scheme the interplanetary impactor (II) scenario. With interplanetary impacts, a steady state is reached between the production of ejecta from the satellite surfaces and the destruction of grains via accretion by the parent moons and Mars itself. We consider successively the dust production rates, the efficiency of dust loss mechanisms, and the dynamical balance between the two.

a. Dust production: Ejecta fluxes from Phobos and Deimos. To model the ejecta yield in different size intervals, we use the technique suggested by Krivov (1994). The idea is to derive the ejecta size distribution from (1) an impactor size distribution and (2) a size distribution of the ejecta produced by a single impactor with a given radius. The former is provided by micrometeoroidal flux models (e.g., Grün *et al.* 1985, Divine 1993). For the latter, we postulate a simple power-law representation determined from the laboratory impact experiments. Provided that the parameters and the cross section of a satellite are known, one can estimate N^+, the cumulative number of grains ejected from the satellite surface per unit time, using the set of equations from Krivov (1994). For the reader's convenience, we reproduce these formulae here explicitly.

Denote by m and M the masses of projectiles and ejecta, respectively, and introduce the following distribution functions: $F(>m)$, the cumulative flux (m^{-2} sec^{-1}) of the interplanetary projectiles more massive than m at the heliocentric distance of Mars; $h(m, M)dM$, the total mass of the ejected particles in the mass range $[M, M + dM]$ produced by a single impact of a projectile with mass m; $g(M)dM$, the total mass of the fragments in the mass range $[M, M + dM]$ ejected from a satellite per unit time; and $N^+(M_1, M_2)$, the cumulative number of grains with $M_1 \leq M \leq M_2$ ejected from the satellite surface per unit time.

According to (Krivov 1994), we have

$$h(m, M) = \begin{cases} (1 - \alpha)\beta^{\alpha-1}Y\,(M/m)^{-\alpha}, & M \leq \beta m, \\ 0, & M > \beta m \end{cases} \quad (4)$$

$$g(M) = -\pi S \int_{m_{min}}^{m_{max}} h(m, M)\frac{dF(>m)}{dm}\,dm, \quad (5)$$

$$N^+(M_1, M_2) = \int_{M_1}^{M_2} M^{-1}\,g(M)dM, \quad (6)$$

where S is the cross section of the satellite. Equations (4)–(6) contain three parameters, Y, α, and β, discussed immediately below. The function $F(>m)$ is taken from the interplanetary meteoroidal flux model (Grün *et al.* 1985), valid in the interval $m_{min} \leq m \leq m_{max}$, with $m_{min} = 10^{-18}$ g and $m_{max} = 10^2$ g.

The first parameter of the impact model, Y, is the characteristic yield (e.g., Canup *et al.* 1993), defined as the ratio of the ejected mass to the projectile mass. For a regolith target and impacts at speeds ≈ 15 km sec^{-1}, we have $Y \approx 1 \times 10^3$ to 5×10^4. These estimates come from cratering impact experiments in the appropriate range of speeds, masses, and material strengths (see, e.g., Lange and Ahrens 1987, Durisen *et al.* 1992, Frisch 1992, Kato *et al.* 1995, Koschny and Grün 1996a,b). We adopt the average:

$$Y = 1 \times 10^4. \quad (7)$$

The second parameter of the impact model, α, is defined as the slope of cumulative mass distribution of the ejecta from a single meteoroid impact. The third parameter, β, is the mass of the largest ejected fragment in projectile mass units. Following the paper on impact experiments cited above (e.g. Koschny and Grün 1996b), we consider $\alpha = 0.5$ to 0.9 and $\beta = 0.1$ to 10 as extreme cases.

Thus the parameters α, β, and Y in our impact model are determined, and the distribution functions in Eqs. (4)–(6) may be evaluated. The calculated ejecta fluxes N^+ for both moons and for various size intervals must then be multiplied by a factor η_{esc}, the fraction of ejected particles that actually escapes the gravitational field of Phobos/Deimos. This factor can be obtained from the ejecta velocity distribution $\Psi(>u) = (u/u_0)^{-\gamma}$ ($u \geq u_0$), where $\Psi(>u)$ is the number of grains with speed greater than speed u. For the surfaces of the martian satellites, we may expect a gently sloping function, with γ between 1.2 and 1.7 and a cutoff velocity u_0 of several meters per second (see, e.g. Frisch 1992). Assuming the pair $u_0 = 10$ m sec^{-1}, $\gamma = 1.7$ as one limiting case and $u_0 = 5$ m sec^{-1}, $\gamma = 1.2$ as the other, the portion of ejecta that escapes from Phobos will be $\eta_{esc} = \Psi(>7.0$ m $sec^{-1}) \sim 0.7$ to 1.0 , where 7.0 m sec^{-1} is the average escape velocity from Phobos' surface (Banaszkiewicz and Ip 1991). For Deimos, $u_{esc} \approx 5.5$ m sec^{-1} (Banaszkiewicz and Ip 1991), so that $\eta_{esc} = \Psi(>5.5$ m $sec^{-1}) \sim 0.9$ to 1.0 . In reality the situation is more complex, especially for Phobos where the escape velocity varies from 3.5 to 15.5 m sec^{-1} over the satellite's surface (Davis *et al.* 1981). Nevertheless, a sizable fraction of the debris should escape so, in the interest of simplicity, we adopt

TABLE I

Dust Production/Ejection Rates N^+ (sec^{-1}) from the Phobos and Deimos Surfaces Assuming an Impact Yield $Y = 1 \times 10^4$ and the Meteoroid Model of Grün *et al.* (1985)[a]

Size range	N^+ (sec^{-1})			
	$\alpha = 0.5, \beta = 0.1$	$\alpha = 0.5, \beta = 10$	$\alpha = 0.9, \beta = 0.1$	$\alpha = 0.9, \beta = 10$
	Phobos			
1–10	3×10^9	4×10^8	1×10^{10}	7×10^9
10–20	2×10^7	6×10^6	1×10^7	1×10^7
20–30	3×10^6	1×10^6	1×10^6	1×10^6
30–35	3×10^5	2×10^5	2×10^5	2×10^5
35–45	4×10^5	3×10^5	2×10^5	2×10^5
45–55	2×10^5	1×10^5	6×10^4	1×10^5
55–70	8×10^4	9×10^4	4×10^4	5×10^4
70–90	4×10^4	5×10^4	1×10^4	3×10^4
	Deimos			
1–5	2×10^9	2×10^8	6×10^9	4×10^9
5–10	6×10^7	1×10^7	6×10^7	4×10^7
10–15	1×10^7	2×10^6	6×10^6	5×10^6
15–20	3×10^6	1×10^6	2×10^6	2×10^6
20–30	2×10^6	6×10^5	7×10^5	7×10^5
30–50	4×10^5	3×10^5	2×10^5	2×10^5
50–70	7×10^4	7×10^4	4×10^4	5×10^4
70–90	2×10^4	3×10^4	6×10^3	2×10^4

[a] Several choices of the model parameters α (the ejecta distribution slope) and β (the largest fragment mass) are shown.

$$\eta_{\text{esc}} = 1 \qquad (8)$$

for both satellites. The ejecta fluxes from Phobos and Deimos covering the size interval $[1, 90\ \mu\text{m}]$ are given in Table I. For further calculations, we adopt the mean values of N^+ obtained by averaging over the columns of Table I.

We stress again that large uncertainties are inevitably present in the above estimates of the impact parameters. These uncertainties arise from (1) an oversimplified model of the impact process and (2) poor knowledge of the surface properties of the martian satellites. A recent, more thorough analysis of spectrophotometric measurements made by the Phobos 2 spacecraft strongly suggests that the Phobos surface is substantially inhomogeneous and consists of "redder" and "bluer" units, neither of which shows direct spectral analogs with any known meteoritic, asteroidal, or laboratory powder materials (Ksanfomality and Moroz 1995, Murchie and Erard 1996). Future missions to observe Phobos and Deimos should give us a better understanding of the surface properties of these small satellites.

b. Dust loss: Lifetimes due to collisions with moons and Mars. We start with a discussion of large particles with radii of tens to hundreds of microns (population I). The dust material of this population is removed primarily via reimpact with the source moon, which acts as a collisional sink (Juhász *et al.* 1993). Thus we need to estimate the relevant collision frequencies.

The collisional time can be evaluated by means of Hamilton and Burns' (1994) Eq. (1). This formula is derived from expressions given by Öpik (1976) and takes into account the dynamics of precessing Keplerian orbits:

$$T^- \approx \pi \sqrt{\sin^2 i + \sin^2 i_{\text{moon}}} \left(\frac{a}{R}\right)^2 \left(\frac{u}{u_r}\right) T, \qquad (9)$$

where i is mean inclination of particle's orbit, i_{moon} is the mean inclination of the moon's orbit (both being measured from Mars' equatorial plane), R and a are the satellite radius and semimajor axis of its orbit, u is the average grain velocity relative to the moon, u_r is the radial component of u; $T = 2\pi\ a/v$ is the orbital period of the particles, and v is the orbital velocity of the moon. The ratio u/u_r weakly depends on the eccentricity and, to 20% accuracy, equals unity; so it can be discarded safely. We also do not make any distinction between the semimajor axes of the grain orbits and that of the satellite.

To use Eq. (9), we need to know the mean inclinations i of different-sized ejecta from both martian moons. We assume that, for Deimos, the inclination changes sinusoidally with time, which has been shown to be the case both numerically and analytically by Hamilton (1996). For

Phobos, the inclination changes in a more complicated manner, but always remains small. We adopt the sinusoidal model for both satellites and calculate the mean inclination: $i = 2/\pi \times i_{max}$, where i_{max} is the size-dependent amplitude of inclination oscillations. The numerical values of i_{max} are given by Krivov et al. (1996b).

To check Eq. (9), we also used the "particle-in-a-box" approximation (Greenberg et al. 1991). In this approach, the reimpact time is given by

$$T^- = \frac{V}{u\pi R^2}, \tag{10}$$

where

$$V = 8\pi a^3 e \sin i \tag{11}$$

is the volume of the torus occupied by the family of Keplerian orbits with a constant semimajor axis a, eccentricity e, inclination i, and with rotating apses and nodes (Kholshevnikov et al. 1993). The random velocity u is calculated as

$$u = na\sqrt{\frac{5}{8}e^2 + i^2}, \tag{12}$$

where n is satellite's mean motion. Again, the mean eccentricities and inclinations developed by the particles are calculated as $e = 2/\pi \times e_{max}$ and $i = 2/\pi \times i_{max}$, with e_{max} and i_{max} taken from Krivov et al. (1996b).

We adopted the following numerical parameters: for Phobos, $R = 12$ km, $a = 9400$ km, $i_{moon} = 1°$, $v = 2.1$ km sec^{-1}; for Deimos, $R = 7$ km, $a = 23500$ km, $i_{moon} = 1°$, $v = 1.35$ km sec^{-1}. The calculated collisional lifetimes and other related quantities are listed in Table II. The results obtained from Eqs. (10)–(12) differ from those calculated from Eq. (9) by less than a factor of 2. For smaller particles (population II), the major loss mechanism is collisions with the central planet. We calculate corresponding lifetimes directly when numerically integrating the equations of motion as described in Section 2. Averaging the values for many trajectories of like-sized particles, we obtained the results given in Table II.

c. Steady-state: Number of particles and optical depth. The steady-state number of particles in a given size interval contained in the torus is

$$N = N^+ T^-, \tag{13}$$

where N^+ is the rate of production of these particles and T^- is their collisional lifetime. Our results for dust production rates, grain lifetimes, and number densities of Phobos and Deimos ring particles, all of which depend on particle sizes, are presented in Table II. These results should be compared with those of Juhász et al. (1993), who gave similar estimates (their Table I) for the Phobos torus. We predict similar lifetimes and torus volumes, but expect somewhat higher dust production rates and therefore larger number densities in the belts. A more serious difference concerns grains with $7\ \mu m \lesssim r_g \lesssim 30\ \mu m$, for which we predict much lower number densities than Juhász et al. (1993) do. We trace this discrepancy to the lack of planetary oblateness in their dynamical model.

A crude estimate of the normal optical depth, $\tau_\perp$, can be obtained in the following way. Let $\tau_\perp$ be the optical depth of the torus when seen from the direction perpendicular to the torus' plane of symmetry. Since the optical depth of a ring, τ, is defined to be the cumulative cross-sectional area of all ring particles found within a unit area (note that τ may be greater than one if ring particles are plentiful), we simply divide the area of all particles in the ring $N\pi r_g^2$ by the area of the ring's azimuthal projection $2\pi a \times 2ae$ to obtain

$$\tau_\perp = \frac{1}{4}\frac{Nr_g^2}{a^2 e}. \tag{14}$$

Similarly, an estimate of the edge-on optical depth of the torus is

$$\tau_\| = \frac{1}{4}\frac{N\pi r_g^2}{a^2 i} = \frac{\pi e}{i}\tau_\perp, \tag{15}$$

where i is measured in radians. For each size range in Table II, we calculate the contribution that grains of that size make toward the ring's total optical depths $\tau_\perp$ and $\tau_\|$. The total optical depths, which are dominated by population I, are also calculated (see Table II). The normal optical depth of the Phobos torus is found to be 1×10^{-8}, but the line-of-sight optical depth may be two orders of magnitude greater, 1×10^{-6}, which favors edge-on observations. The normal and edge-on optical depths of the Deimos torus are less different and amount to 3×10^{-6} and 1×10^{-5}, respectively. All these estimates should not be overinterpreted. Recall again that large uncertainties in the input parameters, most notably in the characteristic yield Y [see Eq. (7) and the preceding discussion], directly translate to uncertainties in calculated optical depths. For example, considering edge-on optical depths of the Phobos ring and Deimos torus, we should more realistically replace the above estimates $\tau_\| = 1 \times 10^{-6}$ (Phobos) and $\tau_\| = 1 \times 10^{-5}$ (Deimos) with inequalities $1 \times 10^{-7} \lesssim \tau_\| \lesssim 5 \times 10^{-6}$ (Phobos) and $1 \times 10^{-6} \lesssim \tau_\| \lesssim 5 \times 10^{-5}$ (Deimos). Our estimates can be compared with optical depths of other dusty rings in the Solar System (e.g. Colwell 1996). The Deimos dust belt may be roughly as dense optically as the jovian dust halo ($\tau_\perp \sim 10^{-6}$) or its gossamer ring ($\tau_\perp \sim$

TABLE II
Parameters of the Phobos and Deimos Tori in the Interplanetary Impactor Scenario[a]

Size range	e	i	N^+	u	V	T^-	N	n	$\tau_\perp$	$\tau_\parallel$
						Phobos				
1–10	0.41	2.8	5×10^9	—	4×10^{11}	0.24	4×10^{16}	1×10^5	3×10^{-10}	7×10^{-9}
10–20	0.41	1.5	1×10^7	—	2×10^{11}	0.69	2×10^{14}	1×10^3	2×10^{-10}	7×10^{-9}
20–30	0.41	0.5	1×10^6	—	7×10^{10}	1.18	4×10^{13}	6×10^2	1×10^{-10}	2×10^{-8}
30–35	0.41	2.1	2×10^5	0.68	3×10^{11}	69 (100)	4×10^{14}	1×10^3	3×10^{-9}	1×10^{-7}
35–45	0.39	0.7	3×10^5	0.65	1×10^{11}	36 (34)	3×10^{14}	3×10^3	4×10^{-9}	4×10^{-7}
45–55	0.38	0.6	1×10^5	0.62	8×10^{10}	34 (28)	1×10^{14}	1×10^3	2×10^{-9}	2×10^{-7}
55–70	0.36	0.4	7×10^4	0.60	6×10^{10}	33 (21)	7×10^{13}	1×10^3	2×10^{-9}	3×10^{-7}
70–90	0.35	0.3	3×10^4	0.58	4×10^{10}	31 (15)	3×10^{13}	8×10^2	2×10^{-9}	3×10^{-7}
Total									1×10^{-8}	1×10^{-6}
						Deimos				
1–5	0.55	11.0	3×10^9	—	3×10^{13}	0.14	1×10^{16}	3×10^2	1×10^{-11}	9×10^{-11}
5–10	0.55	10.6	4×10^7	—	3×10^{13}	0.33	4×10^{14}	1×10^1	8×10^{-12}	8×10^{-11}
10–15	0.55	9.6	6×10^6	—	3×10^{13}	0.63	1×10^{14}	3×10^0	1×10^{-11}	1×10^{-10}
15–20	0.54	25.5	2×10^6	0.83	8×10^{13}	53,000 (59,000)	3×10^{18}	4×10^4	8×10^{-7}	3×10^{-6}
20–30	0.38	18.5	1×10^6	0.59	4×10^{13}	39,000 (42,000)	1×10^{18}	3×10^4	9×10^{-7}	3×10^{-6}
30–50	0.24	10.8	3×10^5	0.36	1×10^{13}	23,000 (42,000)	2×10^{17}	2×10^4	7×10^{-7}	3×10^{-6}
50–70	0.16	6.4	6×10^4	0.23	6×10^{12}	14,000 (16,000)	3×10^{16}	5×10^3	3×10^{-7}	1×10^{-6}
70–90	0.12	3.9	2×10^4	0.16	3×10^{12}	8,700 (11,000)	5×10^{15}	2×10^3	1×10^{-7}	7×10^{-7}
Total									3×10^{-6}	1×10^{-5}

[a] e and i, mean eccentricities and inclinations (with respect to Mars' equatorial plane, in degrees) of particle orbits; N^+, rate of production of the particles by impacts of interplanetary meteoroids (sec^{-1}); u, mean random velocities of torus' particles relative to a parent moon (km sec^{-1}); V, torus volume (km^3); T^-, mean reaccretion time (years); N, total number of grains contained in a steady-state dust torus; $n = N/V$, mean number density (km^{-3}); $\tau_\perp$ and $\tau_\parallel$, estimates of torus' normal and edge-on optical depths [Eqs. (14) and (15)]. The values of T^- for 1- to 30 μm-sized Phobos particles and for 1- to 15-μm Deimos particles are lifetimes against hitting Mars, obtained by numerical integrations. For larger grains, the values of T^- are lifetimes against recollisions with a parent moon, calculated from Eq. (9) and Eqs. (10)–(12) (the latter are enclosed in parentheses).

10^{-7}). It is most likely less dense than Uranus' broad dust bands ($\tau_\perp \sim 10^{-5}$). The dust ring created by interplanetary impacts onto Phobos is probably much fainter than all these structures, except for the case of edge-on observations. Our estimates do not contradict the observational upper limit set by Viking's unsuccessful attempt to detect the dust belts of Mars: $\tau_\perp \lesssim 5 \times 10^{-5}$ (Duxbury and Ocampo 1988).

3.3. Self-Sustained Scenario

In this subsection, we discuss an alternative mechanism which could form and sustain population I of the martian dust cloud. In a study of Saturn's E ring, Hamilton and Burns (1994) first suggested that reimpacts of ring particles with a moon could act as a net source of ring material rather than a sink. Such a ring can sustain itself without the need for an external population of impactors. In the self-sustained (SS) scenario, the equilibrium density of dust is limited by the mutual collisions between the torus grains, rather than by the sweep up of material by the parent moon. Sasaki (1994) pointed out that this mechanism may work in the presumed dust belts of Mars. Later, the idea of self-sustained martian tori was discussed by Hamilton (1996), Ishimoto (1996), and Sasaki (1996a,b).

Equating the rates of dust production (through collisions of the torus particles with the moon) and dust loss (via mutual grain–grain collisions) leads to an estimate of the total number of particles contained in the torus,

$$N = (N_0 - 1)(R/r_g)^2, \tag{16}$$

where N_0 is the number of like-sized grains produced in one reimpact of a torus particle with the parent moon (Sasaki 1994). Substituting (16) into (14) and (15) yields Hamilton's (1996) formula for the normal optical depth of a self-sustained torus,

$$\tau_\perp = (N_0 - 1)\frac{R^2}{4a^2e}, \tag{17}$$

and a formula for the edge-on optical depth,

$$\tau_\parallel = (N_0 - 1)\frac{\pi R^2}{4a^2i}. \tag{18}$$

The key parameter of the SS scenario, N_0, is similar to the characteristic yield Y of an impact that we discussed for the impacts of interplanetary projectiles in Section 3.2.

The mean impact velocity for torus particles is several hundred meters per second (Table II), 20–100 times smaller than typical velocities of interplanetary impactors. The ejecta yield Y is proportional to ν^δ, where ν is the impact velocity and the exponent δ ranges between 2.26 (Frisch 1992) and 2.46 (Koschny and Grün 1996a). Since we adopted $Y \sim 10^4$ for the primary impacts, we expect that $N_0 \approx Y[\nu(\text{torus})/\nu(\text{interplanetary})]^\delta$ may be close to unity.

In an attempt to constrain a possible value of N_0, Sasaki (1996a,b) estimated the erosion rate of the surfaces of the martian satellites. For Phobos and with $N_0 = 2$, ring particles should erode the regolith layer by 10 m in a time scale of Phobos' dynamical evolution due to tidal interaction with Mars, 10^7 years. Since no clear signs of significant erosion have been revealed by spacecraft, it may be that N_0 is significantly smaller than 2; here we take $N_0 = 1.1$ for both satellites. Then we have the following numerical estimates. For Phobos, $N = 2 \times 10^{16}$, $n = N/V = 7 \times 10^4$ km^{-3}, $\tau_\perp = 1 \times 10^{-7}$, and $\tau_\parallel = 4 \times 10^{-6}$. For Deimos, $N = 2 \times 10^{16}$, $n = N/V = 2 \times 10^2$ km^{-3}, $\tau_\perp = 3 \times 10^{-9}$, and $\tau_\parallel = 1 \times 10^{-8}$.

These results are to be compared with expected optical depths in the II scenario: $\tau_\perp = 1 \times 10^{-8}$ and $\tau_\parallel = 1 \times 10^{-6}$ for Phobos and $\tau_\perp = 3 \times 10^{-6}$ and $\tau_\parallel = 1 \times 10^{-5}$ for Deimos. We see that SS mechanism is capable of increasing the dust population in the Phobos torus, even for moderate values of the efficiency N_0. Because of its large volume, however, the Deimos torus is hardly affected by secondary impacts. Only with an unrealistically large $N_0 \gtrsim 100$ will the self-sustaining mechanism dominate the interplanetary impact process in maintaining the dust torus of Deimos.

Unfortunately, the actual value of N_0 is unknown and it may happen that $N_0 \leq 1$; this would mean that the martian tori are not self-sustained. Our present understanding of satellite regoliths and the impact ejecta process is insufficient to decide whether interplanetary impacts or ring particle impacts are the most important source of debris in the martian dust belts.

3.4. Comparison with Other Studies

Our numerical results for number densities and optical depths have been compared with results from 10 recent studies: Juhász et al. (1993), Krivov (1994), Ishimoto and Mukai (1994), Juhász and Horányi (1995), Krivov and Krivova (1996), Hamilton (1996), Ishimoto (1996), Sasaki (1994, 1996a,b). Note that since the first three papers in this list were based on simple dynamical models that did not take into account the effects of Mars' oblateness on particle orbits, the results presented there are less reliable. Nevertheless, we included these papers in our comparative analysis for completeness. Of the 10 papers, Ishimoto and Mukai (1994) discuss only the Phobos torus while Juhász and Horányi (1995) deal with the Deimos belt only. All

TABLE III
Material Densities and Radiation Pressure Efficiencies Adopted in Recent Studies

Reference	ρ_g	Q_{pr}
Juhász et al. (1993)	2.0	1.0
Krivov (1994)	2.0	1.0
Ishimoto and Mukai (1994)	2.4	Size-dep.[a]
Juhász and Horányi (1995)	3.0	0.66[b]
Krivov and Krivova (1996)	2.0	1.0
Hamilton (1996)	2.38	1.0
Ishimoto (1996)	2.4	Size-dep.[c]
Sasaki (1994, 1996a,b)	$\rho_g/Q_{pr} = 2.87$[d]	
This study	2.0	1.0

[a] Q_{pr} is not explicitly given in the paper. We restored it, as a function of r_g, from ρ_g, r_g, and β, the ratio of the radiation pressure force to solar gravity force. For grain radii typical for the tori, Q_{pr} ranges between 0.16 and 0.19.

[b] Private communication by A. Juhász.

[c] See footnote a. Q_{pr} weakly depends on the grain size and is close to 0.4.

[d] ρ_g and Q_{pr} are not explicitly given in the papers. We calculated their ratio from r_g and β.

of the papers consider the large population I particles; while population II is modeled only in Juhász et al. (1993) and in this study. The submicrometer-sized population III grains, which are strongly perturbed by both radiation pressure and electromagnetic forces, are modeled only by Juhász et al. (1993), whose results are based on the earlier modeling of Horányi et al. (1990, 1991).

Prior to a quantitative comparison, we adjust for the fact that different authors work with different values of regolith material density ρ_g and assume different radiation pressure efficiencies Q_{pr} when calculating the radiation pressure force (Table III). Hence the particle sizes and size-related quantities quoted by various authors cannot be directly compared. We use the fact that particles with a given value of $Q_{pr}/(\rho_g r_g)$ are equivalent dynamically (since the relative strength of radiation pressure depends only on this ratio; see, e.g. Burns et al. 1979) to convert all results to a common $\rho_g = 2.0$ g cm^{-3} and $Q_{pr} = 1.00$. For instance, the critical radius of $r_g = 13$ μm for the Deimos particles obtained by Juhász and Horányi (1995) with $\rho_g = 3.0$ g cm^{-3} and $Q_{pr} = 0.66$ translates to $r_g = 30$ μm of Krivov et al. (1996b), who used $\rho_g = 2.0$ g cm^{-3} and $Q_{pr} = 1.00$. Our choices for Q_{pr} and ρ_g are by no means superior to the choices of other authors; they are simply reasonable guesses considering the uncertainties in the properties of the martian satellites.

A compendium of estimated dust belt parameters obtained here and in the papers cited above is given in Table IV. The list of parameters includes the dust production rate in the II scenario and the total number of particles and number density for both II and SS mechanisms. The

TABLE IV
Estimates of Torus Parameters Obtained in Recent Studies[a]

Reference	r'_g	r_g	II scenario				SS scenario			
			N^+	N	n	τ	N_0	N	n	τ
Phobos										
Juhász et al. (1993)										
PopI	10–50	10–50	1×10^6	3×10^{15b}	3×10^{5c}	—	—	—	—	—
PopII	1–6.5	1–6.5	3×10^8	2×10^{15b}	6×10^{3c}	—	—	—	—	—
PopIII	0.1–1	0.1–1	1×10^{11}	8×10^{16b}	1×10^{5c}	—	—	—	—	—
Krivov (1994)	15–50	15–50	—	—	6×10^{4d}	—	—	—	—	—
Ishimoto and Mukai (1994)	$3–7^e$	18–50	1×10^5	—	5×10^{3c}	—	—	—	—	—
Krivov and Krivova (1996)	30–100	30–100	—	—	1×10^{4d}	2×10^{-6h}	—	—	—	—
Hamilton (1996)	$\sim50^f$	~60	—	—	—	—	2	—	1×10^6	8×10^{-7g}
Ishimoto (1996)	$15–32^e$	44–100	—	—	1×10^0	—	2	—	1×10^6	$\leq10^{-5}$
Sasaki (1994, 1996a,b)	$\sim30^f$	~43	—	—	—	—	1.1	2×10^{16}	—	9×10^{-8i}
This study										
PopI	30–55	30–55	6×10^5	8×10^{14}	5×10^{3c}	9×10^{-9g}	1.1	2×10^{16}	7×10^4	1×10^{-7g}
PopII	1–30	1–30	5×10^9	4×10^{16}	1×10^{5c}	6×10^{-10g}	—	—	—	—
Deimos										
Juhász et al. (1993)										
PopI	10–50	10–50	—	—	1×10^{6c}	—	—	—	—	—
PopII	1–6.5	1–6.5	—	—	3×10^{2c}	—	—	—	—	—
PopIII	0.1–1	0.1–1	—	—	5×10^{3c}	—	—	—	—	—
Krivov (1994)	15–50	15–50	—	—	1×10^{5d}	—	—	—	—	—
Juhász and Horanyi (1995)	12–18	27–41	2×10^5	8×10^{16}	5×10^{3d}	4×10^{-8h}	—	—	—	—
Krivov and Krivova (1996)	14–100	14–100	—	—	1×10^{5d}	1×10^{-5h}	—	—	—	—
Hamilton (1996)	$\sim15^f$	~18	—	—	—	—	2	—	—	5×10^{-8g}
Ishimoto (1996)	$7–15^e$	20–44	—	—	1×10^1	—	—	—	—	—
Sasaski (1994, 1996a,b)	$\sim10^f$	~14	—	—	—	—	1.1	5×10^{16}	—	2×10^{-10j}
This study										
PopI	15–50	15–50	3×10^6	4×10^{18}	9×10^{4c}	2×10^{-6g}	1.1	2×10^{16}	2×10^2	3×10^{-9g}
PopII	1–15	1–15	3×10^9	1×10^{16}	3×10^{2c}	3×10^{-10g}	—	—	—	—

[a] r'_g, particle size intervals given in the original papers; r_g, corresponding size intervals scaled to $\rho_g = 2.0$ g cm^{-3} and $Q_{pr} = 1.00$; N^+, dust production rate from the satellite surface (sec^{-1}) (for II scenario) and N_0, characteristic yield for secondary impacts (for SS scenario); N, total number of grains contained in a steady-state dust torus; n, spatial number density of the particles (km^{-3}); τ, estimate of torus' optical depth. The parameters N, n, and τ are given for both scenarios.

[b] Calculated from number density and torus' volume.

[c] Mean number density.

[d] Peak number density.

[e] Calculated from the grain mass and material density.

[f] Typical grain size is given instead of size interval.

[g] Normal optical depth.

[h] Optical depth as seen in the plane of symmetry of the torus.

[i] See footnote h. The formulas derived by the author express τ as a function of mean orbital inclination of the particles. We substituted our value $i = 0.7°$ for 35 to 45-μm Phobos grains (see Table II).

[j] See footnote h. We used $i = 11°$ for 30- to 50-μm Deimos grains (see Table II).

dust grain size intervals are given in two variants: (1) the original sizes used by the authors based on their particular choices for ρ_g and Q_{pr}, and (2) the adjusted sizes that correspond to our standard values $\rho_g = 2.0$ g cm^{-3} and $Q_{pr} = 1.00$. The estimates of the overall optical depths of the belts in both scenarios are also listed in Table IV. Further explanations of the data are given directly in Table IV.

With a few exceptions, results from different authors differ by only one or two orders of magnitude, predicting mean number densities of population I between 5×10^3 and 3×10^5 km^{-3} for the Phobos ring and between 5×10^3 and 1×10^6 km^{-3} for the Deimos torus. Most of these differences are due to uncertainties in the dust production mechanisms, as parameterized by the dust production rate N^+ in the II scenario and the efficiency of impacts N_0 in the SS scenario. This, in particular, is the explanation of the

extremely low dust densities in the II scenario suggested by Ishimoto (1996), who assumed a much smaller value of N^+ than other authors have.

4. CONCLUSIONS

In this paper, we present a new model of the dust belts predicted to exist near the orbits of the martian moons Phobos and Deimos. We use recently obtained dynamical results together with contemporary impact models and employ a new numerical code to construct and visualize a three-dimensional, time-variable, and size-dependent structure of the dust complex near Mars.

Our modeling is divided into two consecutive stages: (1) construction of a relative density distribution and (2) estimation of absolute number densities of the dust material. The first task is solved quite accurately, whereas large (one or even two orders of magnitude) uncertainties are inherent in the solution of the second stage. These uncertainties arise from the fact that regolith properties of the martian satellites and the hypervelocity impact process are still poorly characterized. The unambiguous detection of the martian rings—either by in-situ measurements or by direct imaging from spacecraft—would substantially reduce these uncertainties. Once an unambiguous detection of material orbiting Mars is made at one point in space, number densities and optical depths may be reasonably accurately predicted elsewhere by use of the dynamical model described here.

Our numerical results are available in the form of data tables that provide the expected number densities of different-sized dust grains at locations near the planet for various martian seasons. We also obtain estimates of optical depth and other important parameters of the dust tori, and compare our results with those published by other workers. All these data can be directly used by mission planners in preparation of onboard dust experiments and in assessing the meteoroid hazard to spacecraft during upcoming missions to Mars.

ACKNOWLEDGMENTS

REFERENCES

Andreev, V. V., and O. I. Belkovich 1992. Phobos and Deimos are sources of meteoroids. In *Asteroids, Comets, Meteors 1991*, pp. 9–15. Lunar and Planetary Inst., Tucson, AZ.

Banaszkiewicz, M., and W.-H. Ip 1991. A statistical study of impact ejecta distribution around Phobos and Deimos. *Icarus* **90,** 237–253.

Baumgärtel, K., K. Sauer, A. Bogdanov, E. Dubinin, and M. Dougherty 1996. "Phobos events": Signatures of solar wind dust interaction. *Planet. Space Sci.* **44,** 589–601.

Błęcka, M., and A. Jurewicz 1996. *Toward Finding Out the Dust Rings of Mars: Modeling of an Observational Strategy.* Paper presented at the EGS Meeting, The Hague, May 1996.

Burns, J. A., P. L. Lamy, and S. Soter 1979. Radiation forces on small particles in the Solar System. *Icarus* **40,** 1–48.

Canup, R. M., J. E. Colwell, and M. Horányi 1993. Size distributions of satellite dust ejecta: Effects of radiation pressure and planetary oblateness. *Icarus* **105,** 363–369.

Colwell, J. E. 1996. Size distributions of circumplanetary dust. *Adv. Space Res.* **17**(12), 161–170.

Davis, D. R., K. R. Housen, and R. Greenberg 1981. The unusual dynamic environment of Phobos and Deimos. *Icarus* **47,** 220–233.

Divine, N. 1993. Five populations of interplanetary meteoroids. *J. Geophys. Res.* **98,** 17029–17048.

Dubinin, E. M., R. Lundin, N. F. Pissarenko, S. V. Barabash, A. V. Zakharov, H. Koskinen, K. Schwingenshuh, and Ye. G. Yeroshenko 1990. Indirect evidences for a gas/dust torus along the Phobos orbit. *Geophys. Res. Lett.* **17,** 861–864.

Durisen, R. H., P. W. Bode, J. N. Cuzzi, S. E. Sederbloom, and B. W. Murphy 1992. Ballistic transport in planetary ring systems due to particle erosion mechanisms: II. Theoretical models for Saturn's A- and B-ring inner edges. *Icarus* **100,** 364–393.

Duxbury, T. C., and A. C. Ocampo 1988. Mars: Satellite and ring search from Viking. *Icarus* **76,** 160–162.

Frisch, W. 1992. Hypervelocity impact experiments with water ice targets. In *Proceedings, Workshop on Hypervelocity Impacts in Space* (J. A. M. McDonnell, Ed.), pp. 7–14. Canterbury, GB.

Galeev, A., V. Moroz, V. Linkin, R. Kremnev, G. Rogovsky, K. Pichkhadze, B. Martynov, O. Papkov, A. Eremenko, E. Galimov, Y. Surkov, C. Elachi, R. Bourke, and J. McNamee 1996a. MARS GLOB: Creation of an international network of Mars surface landers. *Adv. Space Res.* **17**(12), 15–20.

Galeev, A. A., V. I. Moroz, V. M. Linkin, A. V. Zakharov, A. T. Basilevsky, Yu. A. Surkov, E. L. Akim, T. Duxbury, R. S. Kremnev, B. N. Martynov, and O. V. Papkov 1996b. Phobos sample return mission. *Adv. Space Res.* **17**(12), 31–47.

Greenberg, R., W. F. Bottke, A. Carusi, and G. B. Valsecchi 1991. Planetary accretion rates—Analytical derivation. *Icarus* **94,** 98–111.

Grün, E., H. A. Zook, H. Fechtig, and R. H. Giese 1985. Collisional balance of the meteoritic complex. *Icarus* **62,** 244–272.

Hamilton, D. P. 1996. The asymmetric time-variable rings of Mars. *Icarus* **119,** 153–172.

Hamilton, D. P., and J. A. Burns 1994. Origin of Saturn's E ring: Self-sustained, naturally. *Science* **264,** 550–553.

Hamilton, D. P., and A. V. Krivov 1996. Circumplanetary dust dynamics: Effects of solar gravity, radiation pressure, planetary oblateness, and electromagnetism. *Icarus* **123,** 503–523.

Horányi, M., J. A. Burns, M. Tátrallyay, and J. G. Luhmann 1990. Toward understanding the fate of dust lost from the martian satellites. *Geophys. Res. Lett.* **17,** 853–856.

Horányi, M., M. Tátrallyay, A. Juhász, and J. G. Luhmann 1991. The dynamics of submicron-sized dust particles lost from Phobos. *J. Geophys. Res.* **96**, 11283–11290.

Huntress, W. T., Jr, T. J. Feeley, and J. M. Boyce 1996. NASA's strategy for Mars exploration in the 1990s and beyond. *Adv. Space Res.* **17**(12), 7–14.

Ip, W.-H., and M. Banaszkiewicz 1990. On the dust/gas tori of Phobos and Deimos. *Geophys. Res. Lett.* **17**, 857–860.

Ishimoto, H. 1996. Formation of Phobos/Deimos dust rings. *Icarus* **122**, 153–165.

Ishimoto, H., and T. Mukai 1992. Dynamics of small particles ejected from Phobos. In *Proceedings, XXVth Symposium on Celestial Mechanics* (H. Kinoshita and H. Nakai, Eds.), pp. 39–43. Tokyo.

Ishimoto, H., and T. Mukai 1994. Phobos dust rings. *Planet. Space Sci.* **42**, 691–697.

Ishimoto, H., H. Kimura, N. Nakagawa, and T. Mukai 1997. Planned observation of Phobos/Deimos dust rings by Planet-B. *Adv. Space Res.* **19**(1), 123–126.

Juhász, A., and M. Horányi 1995. Dust torus around Mars. *J. Geophys. Res.* **100**(E2), 3277–3284.

Juhász, A., M. Tátrallyay, G. Gévai, and M. Horányi 1993. On the density of the dust halo around Mars. *J. Geophys. Res.* **98**, 1205–1211.

Kato, M., Y. Iijima, M. Arakawa, Y. Okimura, A. Fujimura, N. Maeno, and H. Mizutani 1995. Ice-on-ice impact experiments. *Icarus* **113**, 423–441.

Kholshevnikov, K. V., A. V. Krivov, L. L. Sokolov, and V. B. Titov 1993. The dust torus around Phobos orbit. *Icarus* **105**, 351–362.

Koschny, D., and E. Grün 1996a. Impacts into ice–silicate mixtures: Crater morphologies, volumes, depth-to-diameter ratios and yield. *Icarus.* [Submitted]

Koschny, D., and E. Grün 1996b. Impacts into ice–silicate mixtures: Ejecta mass and size distributions. *Icarus.* [Submitted for publication]

Krivov, A. V. 1994. On the dust belts of Mars. *Astron. Astrophys.* **291**, 657–663.

Krivov, A. V., and N. A. Krivova 1996. Expected features of martian dust belts. In *Proceedings, IIIrd Internaitonal Workshop on Positional Astronomy and Celestial Mechanics* (A. Lopez Garcia *et al.*, Eds.), pp. 235–244. Astronomical Observatory, University of Valencia.

Krivov, A. V., and V. B. Titov 1994. The dust torus of Phobos. In *Dynamics and Astrometry of Natural and Artificial Celestial Bodies* (K. Kurzyń-

ska *et al.*, Eds.), pp. 281–286. Astronomical Observatory of A. Mickiewicz University, Poznań.

Krivov, A. V., L. L. Sokolov, and V. V. Dikarev 1996a. Dynamics of Mars-orbiting dust. In *Proceedings, IIIrd International Workshop on Positional Astronomy and Celestial Mechanics* (A. Lopez Garcia *et al.*, Eds.), pp. 225–234. Astronomical Observatory, University of Valencia.

Krivov, A. V., L. L. Sokolov, and V. V. Dikarev 1996b. Dynamics of Mars-orbiting dust: Effects of light pressure and planetary oblateness. *Celest. Mech. Dynam. Astron.* **63**, 313–339.

Krivov, A. V., L. L. Sokolov, K. V. Kholshevnikov, and V. A. Shor 1991. On the existence of a swarm of particles in the vicinity of the Phobos orbit. *Solar Syst. Res.* **25**, 233–242.

Krymskii, A. M., T. K. Breus, M. K. Dougherty, D. J. Southwood, and W. I. Axford 1992. The electromagnetic effects of the solar wind interaction with the Phobos neutral gas halo and dust torus. *Planet. Space Sci.* **40**, 1033–1041.

Ksanfomality, L. V., and V. I. Moroz 1995. Spectral reflectivity of Phobos' regolith within the range 315–600 nm. *Icarus* **117**, 383–401.

Lange, M., and T. Ahrens 1987. Impact experiments in low-temperature ice. *Icarus* **69**, 506–518.

Murchie, S., and S. Erard 1996. Spectral properties and heterogeneity of Phobos from measurements by Phobos 2. *Icarus.* **123**, 63–86.

Öpik, E. J. 1976. *Interplanetary Encounters: Close-Range Gravitational Interactions.* Elsevier, New York.

Orofino, V., J. Grygorczuk, and A. Jurewicz 1997. Photometry of the martian dust rings. *Planet. Space Sci.* [Submitted for publication]

Sasaki, S. 1994. Martian dust tori formation: Ejecta at collision of torus particles with the satellite can sustain the dust abundance. In *Proceedings, 27th ISAS Lunar and Planetary Symposium* (M. Shimitzu and H. Mizutani, Eds.), pp. 47–50.

Sasaki, S. 1996a. Phobos and Deimos as sources of martian dust ring/torus. *Lunar Planet. Sci. Conf. 27th,* 1127–1128.

Sasaki, S. 1996b. Martian self-sustaining dust torus. In *Proceedings, IAU Colloquium No. 150: Physics, Chemistry, and Dynamics of Interplanetary Dust* (B. Å. S. Gustafson and M. S. Hanner, Eds.), pp. 187–190.

Soter, S. 1971. The dust belts of Mars. Report of Center for Radiophysics and Space Research No. 462. Cornell Univ., Ithaca, NY.

Tátrallyay, M., M. Horányi, A. Juhász, and J. G. Luhmann 1992. Submicron-sized dust grains in the martian environment. *Adv. Space Res.* **12**, 27–30.

Tsuruda, K., I. Natakani, and T. Yamamoto 1996. Planet-B mission to Mars—1998. *Adv. Space Res.* **17**(12), 21–29.